JNeurosci
THE JOURNAL OF NEUROSCIENCE

Research Articles: Behavioral/Cognitive

Beta bursting in the retrosplenial cortex is a neurophysiological correlate of environmental novelty which is disrupted in a mouse model of Alzheimer's disease

https://doi.org/10.1523/JNEUROSCI.0890-21.2022

Cite as: J. Neurosci 2022; 10.1523/JNEUROSCI.0890-21.2022

Received: 26 April 2021
Revised: 15 July 2022
Accepted: 18 July 2022

Beta bursting in the retrosplenial cortex is a neurophysiological correlate of environmental novelty which is disrupted in a mouse model of Alzheimer's disease.

Beta bursting in the retrosplenial cortex

Callum Walsh, Thomas Ridler, Gabriella Margetts-Smith, Maria Garcia Garrido, Jonathan Witton, Andrew D. Randall, Jonathan T. Brown

Institute of Biomedical and Clinical Sciences, University of Exeter Medical School, Hatherly Laboratories, Exeter EX4 4PS, United Kingdom

Corresponding Authors: C. Walsh, cw685@exeter.ac.uk, J. T. Brown, J.T.Brown@exeter.ac.uk

Figures: 13

Abstract: 224 words

Introduction: 643 words

Discussion: 1488 words

Conflict of Interest Statement

The authors declare no competing financial interests or conflicts of interest.

Acknowledgements

CFW was funded by a University of Exeter and Janssen Pharmaceutica studentship. TR was supported by an ARUK Major Project grant (ARUK-PG2017B-7) awarded to JTB and AR.

Abstract

The retrosplenial cortex (RSC) plays a significant role in spatial learning and memory and is functionally disrupted in the early stages of Alzheimer's disease. In order to investigate neurophysiological correlates of spatial learning and memory in this region we employed *in vivo* electrophysiology in awake and freely moving male mice, comparing neural activity between wild-type and J20 mice, a transgenic model of Alzheimer's disease-associated amyloidopathy. To determine the response of the RSC to environmental novelty local field potentials were recorded while mice explored novel and familiar recording arenas. In familiar environments we detected short, phasic bursts of beta (20-30 Hz) oscillations (beta bursts) which arose at a low but steady rate. Exposure to a novel environment rapidly initiated a dramatic increase in the rate, size and duration of beta bursts. Additionally, theta-alpha/beta cross-frequency coupling was significantly higher during novelty, and spiking of neurons in the RSC was significantly enhanced during beta bursts. Finally, excessive beta bursting was seen in J20 mice, including increased beta bursting during novelty and familiarity, yet a loss of coupling between beta bursts and spiking activity. These findings support the concept that beta bursting may be responsible for the activation and reactivation of neuronal ensembles underpinning the formation and maintenance of cortical representations, and that disruptions to this activity in J20 mice may underlie cognitive impairments seen in these animals.

Significance Statement

The retrosplenial cortex is thought to be involved in the formation, recall and consolidation of contextual memory. The discovery of bursts of beta oscillations in this region, which are associated with increased neuronal spiking and strongly upregulated while mice explore novel environments, provides a potential mechanism for the activation of neuronal ensembles, which may underlie the formation of cortical representations of context. Excessive beta bursting in the retrosplenial cortex of J20 mice, a mouse model of Alzheimer's disease, alongside the disassociation of beta bursting

from neuronal spiking, may underlie spatial memory impairments previously shown in these mice. These findings introduce a novel neurophysiological correlate of spatial learning and memory, and a potentially new form of Alzheimer's disease related cortical dysfunction.

Introduction

The retrosplenial cortex (RSC) is considered to play a critical role in spatial learning and memory. Damage to this region results in severe impairments in navigation and landmark processing (see Mitchell *et al.*, 2018 for review). There is a large body of experimental evidence suggesting the retrosplenial cortex is involved in the encoding, retrieval and consolidation of spatial and contextual memory (see Todd and Bucci, 2015 for review). Optogenetic stimulation of RSC neurons is sufficient to elicit retrieval and consolidation of contextual memories (Cowansage et al., 2014; De Sousa et al., 2019). RSC neurons encode a range of contextual information during navigation, and inactivation of the RSC using glutamate receptor antagonists impairs performance in the Morris water maze and contextual fear memory tasks (Czajkowski et al., 2014; Kwapis et al., 2015), suggesting the RSC is involved in the storage of spatial information. Finally, Iaria *et al.* (2007) demonstrated that while hippocampal subregions are differentially involved in the encoding and retrieval of spatial information, the entire RSC is active during both processes. Spatial learning and memory impairments have been shown to be one of the earliest aspects of cognitive impairment in Alzheimer's disease (AD). Patients exhibit disturbances in specific spatial memory processes associated with the RSC (Laczó et al., 2009; Vann et al., 2009; Morganti et al., 2013). During the early stages of AD, the retrosplenial gyrus has been shown to exhibit regional hypometabolism (as measured by FDG-PET), and considerable atrophy (Minoshima et al., 1997; Choo et al., 2010). As such, the RSC is a region of great interest in research into the brain's function in health and AD.

Measurable correlates of brain function can have great value in fundamental neuroscience. They can aid the understanding of the complex ways in which the brain processes information and performs its many tasks and indicate how such functionality may be affected in disease. Similarly, these "functional biomarkers" can provide measurable benchmarks against which to test interventions

which may affect or restore normal brain function (Walsh et al., 2017). Of the growing number of methodologies available for investigating brain function, *in vivo* electrophysiology remains a powerful tool with a superior temporal resolution to all others. The coordinated firing of large groups of neurons in the brain gives rise to waves of electrical activity, known as neural oscillations, which can be recorded as intracranial local field potentials (LFPs) or extracranial electroencephalograms (EEGs). It is thought that one of the roles of these oscillations in the brain is to coordinate the spiking activity of neurons, allowing computation and communication between potentially distant brain regions (Canolty et al., 2010). The temporal resolution of electrophysiology combined with the spatial specificity afforded by intracranial recordings make *in vivo* electrophysiology an invaluable tool for discovering functional correlates of brain function and disease-associated dysfunction.

In order to investigate the function of the RSC in spatial learning and memory, we recorded LFPs and multi-unit spiking activity from this region, while mice freely explored either a novel or familiar environment. To probe the effects of AD-associated amyloid pathology on RSC function we used J20 mice, a widely employed mouse model of amyloidopathy. In this paper, we describe short, phasic bursts of beta (20-30 Hz) oscillations, termed “beta bursts”, that occur within the RSC, while mice freely explore an environment. Beta bursting activity is significantly increased during exposure to a novel environment, and these bursts are correlated with increased neuronal spiking in the RSC. These data demonstrate that beta bursting in the RSC is a robust neurophysiological correlate of environmental novelty and may have a role in the storage and retrieval of cortical spatial representations. Finally, we observed excessive beta bursting activity and an uncoupling of beta bursting from neuronal spiking in the RSC in J20 mice, which may disrupt its function, and underlie spatial learning and memory deficits seen in these mice (Cheng et al., 2007).

Methods

Ethics

All procedures were carried out in accordance with the UK Animal (Scientific Procedures) Act 1986 and were approved by the University of Exeter Animal Welfare and Ethical Review Body.

Animals

8 male J20 mice and 5 wild-type littermates were bred in-house at the University of Exeter and housed on a 12-hour light/dark cycle. This sample size was estimated from a similar previous study performed by one of the authors (Ahnaou et al., 2019), and proved to be sufficient for this study. J20 mice were bred on a C57BL/6 background. Access to food and water was provided ad libitum. All mice underwent surgery at between 6-8 months-of-age. Mice were group housed prior to surgery, and single housed post-surgery, in order to prevent damage to the surgical implants.

Surgery

Mice were unilaterally implanted with a 16 channel, single shank silicon probe (NeuroNexus Technologies, A1x16-5mm-100-177-CM16LP), in the right retrosplenial cortex (AP –2 mm, ML +0.5 mm, DV +1.75 mm, 0° Pitch). Mice were anaesthetised using isoflurane and fixed into a stereotaxic frame. A small craniotomy was drilled over the desired co-ordinate, and at least one hole was drilled in each of the major skull plates, in which miniature screws were placed to act as supports (Antrin Miniature Specialties). The probe was slowly lowered into the desired location, and fixed in place with dental cement (RelyX Unicem, 3M). The ground wire from the probe was connected to a silver wire, attached to a screw overlying the cerebellum. Throughout surgery, body temperature was monitored with a rectal probe and regulated by a feedback-controlled heat mat. Animals were kept hydrated by subcutaneous injections of Hartmann's solution once per hour of surgery (0.01 ml/g body weight).

Behaviour

After at least one week of post-surgical recovery, animals underwent a Novel/Familiar environment task, as shown in (Fig. 1). Individual mice were tethered to the recording apparatus and placed in one of two high-sided recording arenas: one square, with black and white stripes, and one circular and lacking stripes. Both arenas each had two internal visual cues, placed on opposite sides. The

animals were allowed to freely explore their environment for 15 minutes, after which, they were returned to their home cage. After 15 minutes in their home cage, the animal was returned to the same recording arena for another 15 minutes and allowed to freely explore. Following this, the animal was returned to its home cage. This protocol was repeated at the same time of day, for 5 consecutive days, but on the fifth day, the animal was placed in the other, previously unseen arena. The order of exposure to these arenas was counterbalanced between animals. Each session can therefore be described by the experimental day, and the particular session within that day, with session A being the first, and session B being the second. Using this nomenclature, Sessions 1a and 5a were 'novel' sessions, while the remaining sessions were 'familiar' sessions. In order to reduce the stress associated with the recording process, animals were acclimatised to this process during 10-minute test session 3 days prior to the start of the experiment, in which the animal was tethered and recorded from while in its home cage. An added benefit of this was to familiarize the animals with this experimental procedure, thus ensuring that perceived novelty during the first experimental session was limited to the environment, and not the experience of being tethered to the recording apparatus.

Data Collection

Throughout experimental sessions, Local Field Potentials (LFPs) were recorded using an Open Ephys Acquisition board (Open Ephys), which was tethered to the probe via a headstage (RHD 16-Channel Recording Headstage, Intan Technologies), and SPI cables (Intan Technologies). LFPs on each channel were sampled at 30 kHz, while the animal's location was monitored using a pair of light-emitting diodes (LED) soldered to the headstage, and a video camera (Logitech HD Pro Webcam C920, Logitech), placed directly above the arena. The location of these LEDs was tracked at 30 frames per second using Bonsai tracking software, so the location and running speed of the animal could be estimated offline. To reduce noise, position information was smoothed using a Savitzky-Golay filter of order 3 and running speed was calculated on a second-by-second basis.

Data Analysis

LFPs were down-sampled (Spectral Analysis: 1 kHz, Burst Detection and Phase Amplitude Coupling: 3 kHz, Multi-Unit Activity: 30 kHz) and de-trended, in order to remove any slow linear drift of the baseline that may occur across the session. The Chronux toolbox (Mitra and Bokil, 2008, http://chronux.org/) was used for the mtspecgramc function, as well as the CircStat toolbox for circular statistics (Berens, 2009). Several built-in MATLAB functions were used as well as some functions from the MATLAB File Exchange including shadedErrorBar (Campbell, 2021) and polyfitZero (Mikofski, 2021). All other scripts used in this study were written in-house and will be made publicly available (see Software Accessibility). All LFP analyses were performed for a single channel located in the centre of the dysgranular RSC. In order to select channels which were at equivalent depths between animals, a combination of post-hoc histology and functional outputs were used to determine the exact locations of each channel. One functional output makes use of the fact that the phase of theta oscillations reverses across the pyramidal cell layer of the hippocampus, so for probes which reached or crosses this layer, it is possible to work backwards to find the exact location of each channel to less than 100 μm.

Power Spectra

Multi-taper spectral analysis was performed using the mtspecgramc function from the Chronux Toolbox, with a time-bandwidth product of 2 (1 second x 2 Hz), and 3 tapers, resulting in some smoothing of resulting spectra. The mtspecgramc function generates a power spectrogram by generating multiple power spectra for short segments of time series data, using a moving window; in our case with the window size of 1 s with no overlap. These spectrograms were then logged to the base 10, and multiplied by 10, in order to correct for the tendency of spectral power to decrease with a 1/f distribution. These individual spectra were averaged, resulting in a single mean power spectrum for the entire session, or for the first minute of each session, as specified in the results. Spectral data from 48 to 52 Hz, which incorporates line frequency noise (50 Hz), were removed, and linearly interpolated. The power of each frequency band was calculated as the mean power in each of the following frequency ranges: delta (1-5 Hz), theta (5-12 Hz), alpha (12-20 Hz), beta (20-30 Hz)

and gamma (30-100 Hz). Wavelet analysis was performed using the cwt function in MATLAB, with the Morlet wavelet with equal variance and time and frequency. The scale to frequency conversions are set by the sampling rate of 30 kHz.

Beta Burst Detection

The data were band-pass filtered between 20-30 Hz, to isolate the beta frequency band, using a Butterworth IIR filter with an order of 2. The amplitude and phase of this beta signal were calculated as the real and imaginary components of the Hilbert transform, respectively. The amplitude was z-scored, in order to give the instantaneous standard deviation of the beta signal amplitude from the mean. Epochs of the signal where this z-score exceeded 2 standard deviations from the mean amplitude were detected, as were the corresponding "edges" of these epochs, where the signal magnitude surpassed 1 standard deviation either side of the 2 standard deviation threshold. This was done in order to capture the time-course of these high beta amplitude epochs. Events that did not persist longer than a minimum duration of 150 ms (i.e. fewer than 3 oscillation cycles) were discarded. Furthermore, due to the sensitivity of this method to large, amplitude noise artefacts, any event whose peak amplitude exceeded three scaled median absolute deviations from the median of the events detected in that session were discarded as well. These remaining events were then considered beta-bursts. The duration and peak magnitude of each burst was calculated, as well as the distribution and total number of bursts in the session. Running speed during beta bursts was estimated as the animal's instantaneous running speed at the time of the beta burst.

Phase-Amplitude Coupling

To calculate phase-amplitude coupling, and create phase-amplitude coupling comodulograms, modulation index (MI) was calculated individually for each pair of phase and amplitude frequencies as described by Tort et al. (2009). This method has been shown to be superior to alternative methods and is less sensitive to changes in amplitude. A full explanation of this method can be found in (Tort et al., 2009), but will be briefly explained here. Phase-amplitude coupling was calculated between phase frequencies in bins of 0.25 Hz from 2 to 12 Hz, and amplitude frequencies in bins of 2

Hz from 10 to 100 Hz. For each pair, local field potentials were filtered in the phase frequency band and the amplitude frequency band, using a Butterworth IIR filter with an order of 2, after which the instantaneous phase and amplitude of each filtered signal was calculated, respectively, using the Hilbert transform. The phases of the "phase signal" were binned in 10° bins, and the average amplitude of the "amplitude signal" was calculated for each phase bin, after which this "amplitude distribution" was normalised so that the sum of all bins is equal to 1. The existence of phase-amplitude coupling can be seen in these amplitude distributions as a non-uniform amplitude across the phase bins, and as such, the Kullback-Leibler distance was calculated to quantify the divergence of this amplitude distribution from the uniform distribution (Kullback and Leibler, 1951). In order to convert to Kullback-Leibler distance to Modulation Index, with a scalar value between 0 and 1, this value is divided by the natural logarithm of the number of phase bins, which in this case is 18. Although this method is far less sensitive to spurious coupling than other methods, we still normalised the resulting modulation index. This was done by the generation of 100 surrogates, where the data was time shifted by a random amount between 1 and 59 seconds, for which the modulation index was calculated. A gaussian distribution was then fitted to these surrogate modulation indexes and the actual modulation index was calculated as a z-score from the mean of this distribution. This same mathematical operation was performed for all phase and amplitude frequency pairs to create a comodulograms, and in order to smooth the resulting comodulograms, the data matrix was linearly interpolated in both dimensions by a factor of 2.

Multi-Unit Activity

Due to the distance between adjacent channels on the recording probe (100 µm) it is highly unlikely that activity of a single neuron would appear on multiple channels. Consequently, each channel was treated as an individual multi-unit. Raw local field potentials were first common average-referenced, using a mean of the signals from all other 15 channels, then filtered in the range of 500-14250 Hz, using a Butterworth IIR filter with an order of 4, in order to isolate the spiking frequency band. Spikes were detected as peaks that crossed a threshold given by the median of the absolute voltage

values of the signal, multiplied by 0.6745, as suggested by Quiroga, Nadasdy and Ben-Shaul (2004), and had a minimum separation of 0.5 ms. In order to investigate multi-unit activity during beta bursts, bursts were detected as previously mentioned, and bursts that occurred within a second of each other were discarded, to remove overlapping segments. Peri-event histograms were created by counting the total number of spikes in 50 ms time bins from 0.5 seconds before burst onset, to 0.5 seconds after, for all beta bursts. Each histogram was then normalised by dividing the count in each bin by the total number of spikes in all bins, averaged across all beta bursts, and then across all sessions and z-scored with respect to the baseline epoch (0.5 seconds pre-burst). Potential phase-locking of spikes to beta oscillations was investigated using circular statistics in a manner similar to Siapas et al.(2005). All spikes in a session were binned depending on the instantaneous phase of the beta oscillation at which they occurred and then counted to produce a phase-distribution histogram. The Rayleigh test was then performed to statistically test for non-uniformity in these distributions, which would be indicative of phase-locking to a specific phase of the beta oscillation. Rayleigh's Z statistic gives the significance level of this test, and any sessions with a Z statistic equivalent to $p < 0.05$ were considered to demonstrate significant beta phase-locking. The μ and κ parameters were estimated from the von Mises distribution to determine the preferred phase and concentration (strength) of this beta phase-locking, respectively.

Software Accessibility

All code has been made publicly available at https://github.com/cfle/In-Vivo-Ephys-Code. This code is freely accessible for viewing, or use. If using any of this code in a paper, please, cite this paper as well as the GitHub repository (https://github.com/cfle/In-Vivo-Ephys-Code).

Statistics

All statistical analysis was performed in MATLAB. Thirteen mice in total were used in this study, 5 wild-type and 8 J20, with each mouse undergoing a total of ten recording sessions (5 days, 2 sessions per day). Unfortunately, the local field potential data from Day 3 session 1 (i.e. session 3a) was corrupted for a single wild-type mouse, and therefore data for this mouse from this session was

omitted from all figure making and statistics. Therefore, the n numbers for all statistics are (wild-type: n = 5 (except from Day3a where n = 4), J20: n = 8). All statistical analysis was performed in MATLAB using several different built-in functions. Statistical analysis varied depending on the type of analysis performed, however most of the statistical analysis was performed using mixed ANOVA with varying number of factors. The Novel/Familiar environment task involved 2 novel sessions and 8 familiar sessions, so in order to account for this imbalance, data was averaged across all novel and all familiar sessions. For most analyses, mixed ANOVAs had two factors, with genotype as the between-subjects factor, and novelty as the within-subjects factor. Other additional factors included region or age. Significant main effects or interactions from an ANOVA was subsequently followed up with relevant planned comparisons. Statistical tests used for each analysis are noted alongside the results of that analysis, throughout this paper.

Histology and Amyloid Plaque Staining

Upon completion of the experiments, mice were killed using an overdose of sodium pentobarbital (Euthetal), and an isolated stimulator was used to produce electrolytic lesions at the recording sites. Mice were then transcardially perfused with 4% paraformaldehyde (PFA), and their brains were extracted and stored in PFA for 24 hours, after which they were transferred to phosphate-buffered saline (PBS) prior to sectioning. Brains were sliced into 100 µm sagittal sections using a vibratome (Leica), and stained with Cresyl Violet. Digital pictures were taken using QCapture Pro 7 software (Qimaging), and electrode sites were verified by comparing the lesion sites in these photographs to The Allen Mouse Brain Atlas (https://mouse.brain-map.org/static/atlas). Due to the high channel count of these probes, as well as their linear geometry, it was possible to account for small differences in the depth of each probe by selecting channels of similar depths across different probes. This resulted in reduced variability between animals in a range of neurophysiological measures.

Amylo-Glo staining was performed on formalin fixed slices according to the recommended protocol. 70% ethanol solution was applied to the slices for 5 minutes, after which the slices were rinsed in

distilled water for 2 minutes. 100X Amylo-Glo stock solution was diluted 1:100 using 0.9% saline solution, and slices were then incubated in this 1X solution for 10 minutes. After this they were rinsed in 0.9% saline solution for 5 minutes, and then distilled water for approximately 15 seconds, before cover slipping with Dako Fluorescence Mounting Medium (Dako). Imaging of plaques was performed on a confocal microscope (ThorLabs), or a Nikon Eclipse E800 Fluorescence Microscope (Nikon).

Parvalbumin Staining

Mice were terminally anaesthetised with an intraperitoneal injection of sodium pentobarbital (Euthetal) before being transcardially perfused (5 ml/min) with phosphate buffered saline (PBS) followed by 4% paraformaldehyde (PFA) in PBS. Following the perfusion the brains were extracted and stored in 4% PFA for 22 hours at 4°C, then cryoprotected in 30% Sucrose in PBS-Azide (PBS, 0.02% sodium azide) for at least 3 days. Using a freezing sledge microtome, (Leica SM2010R with Physitemp BFS-5MP temperature controller) 30 µm coronal sections were taken from frozen brains (-20°C) and stored in cryoprotectant solution (25% glycerol, 30% ethylene glycol, 25% 0.2 M Phosphate buffer, 20% ddH2O) at -20°C.

For parvalbumin staining, all steps were conducted at room temperature unless stated otherwise. 30 µm free-floating sections stored in cryoprotectant solution were washed in PBS (3x 10 minutes), before being incubated in PBS with 0.09% hydrogen peroxide for 20 minutes to quench endogenous peroxidase. Next, sections were washed in PBS (3x 10 minutes), then blocked and permeabilised in PBS-Tx (PBS, 0.2% Triton X-100) with 3% normal goat serum (NGS) (Vector Laboratories, S-1000). The sections were then incubated in 1:5000 rabbit anti-PV primary antibody (Swant, PV27) in PBS-Tx with 3% NGS at 4°C overnight. The following day the sections were washed in PBS (3x 10 minutes), then incubated for 2 hours in 1:600 goat biotinylated anti-rabbit secondary antibody (Vector Laboratories, BA-1000) in PBS-Tx with 1% NGS. Sections were washed in PBS (2x 10 minutes), then incubated in an Avidin-Biotin complex solution (Vector Laboratories, PK-4000) for 1 hour. After a further three washes in PBS, the sections were incubated with 0.04% 3,3'-Diaminobenzidine-tetrahydrochloride

(DAB) (Hello Bio, HB0687) with 0.04% hydrogen peroxide and 0.05% ammonium nickel(II) sulfate (Merck Life Sciences, A1827) in PBS for approximately 10 minutes. After a final two washes in PBS, sections were mounted on Superfrost Plus slides (Fisherbrand) and left to dry overnight. The next day, sections were serially dehydrated in graded ethanol baths and then cleared in Histo-Clear II (Scientific Laboratory Supplies, NAT1334) for 20 minutes. Slides were then sealed and coverslipped using Histo-Mount mounting medium (Scientific Laboratory Supplies, NAT1310).

Semi-automated cell counting was performed using Fiji (Schindelin et al., 2012). Briefly, images at 10X magnification were locally thresholded using the Sauvola method, in order to account for potential differences in brightness across the image. The image was then despeckled and eroded to remove noise, and cells were automatically counted using the Analyze Particles function. These results were manually checked in order to remove clearly spurious detections, and then the number of cells in each subregion of the retrosplenial cortex were counted. Analysis was performed fully blinded with regards to genotype.

Results

To investigate neurophysiological correlates of spatial learning and memory in the retrosplenial cortex (RSC), local field potentials were recorded from across the entire dorsoventral axis of the RSC, while animals underwent a novel/familiar environment task. The RSC is made up of two distinct subdivisions: dysgranular (RSCdg), and granular (RSCg), however for this study we focused on recordings from the dysgranular RSC (Fig. 1c, channel shown in red).

Spectral Analysis

Local field potentials from RSCdg show a clear peak in theta frequency band (5-12 Hz) throughout recording sessions (Fig. 2a), as well as smaller peaks at higher frequencies. In order to investigate any changes in oscillatory activity in RSCdg during environmental novelty, power spectral analysis was performed on the entire 15 minutes of each session. These power spectra were averaged across novel and familiar sessions for wild-type and J20 mice. Gamma power was significantly higher overall during novel sessions (Gamma: Main Effect Novelty - $F(1,11) = 21.6$, $p = 7e\text{-}4$, Mixed ANOVA).

Gamma power was significantly higher during novel sessions in wild-type (Nov: 10.6 ± 0.1 dB; Fam: 10.2 ± 0.1 dB, p = 0.01) and J20 mice (Nov: 11.2 ± 0.2 dB; Fam: 10.8 ± 0.2 dB, p = 0.004). There were significant interactions between the effects of genotype and novelty on delta, alpha and beta power (Delta: Interaction - $F(1,11) = 9.4$, $p = 0.01$, Mixed ANOVA; Alpha: Interaction - $F(1,11) = 6$, $p = 0.03$, Mixed ANOVA; Beta: Interaction - $F(1,11) = 5.2$, $p = 0.04$, Mixed ANOVA). Delta power was significantly higher during familiar sessions in wild-type (Nov: 22.1 ± 0.7 dB; Fam: 22.5 ± 0.7 dB, p = 0.02), but not J20 mice. Beta power was significantly higher during novel sessions in both wild-type (Nov: 14.2 ± 0.2 dB; Fam: 13.7 ± 0.2 dB, p = 0.02) and J20 mice (Nov: 16.7 ± 0.3 dB; Fam: 15.8 ± 0.3 dB, p = 2e-5). Moreover, beta power was significantly higher in J20 mice than in wild-type mice, for both novel (Nov - WT: 14.2 ± 0.2 dB; J20: 16.7 ± 0.3 dB, p = 0.001) and familiar sessions (Fam - WT: 13.7 ± 0.2 dB; J20: 15.8 ± 0.3 dB, p = 0.002). Upon closer inspection of power spectrograms (Fig. 2a), it was clear that spectral activity changed within novel sessions. Power in the alpha, beta and low gamma range appeared to be higher in the first minute of the session and diminish over time. As exemplified in (Fig. 2c), transient epochs of high power in the 12-40 Hz range are seen throughout the early stages of the session. By performing the same power spectral analysis as before on only the first minute of each session, clear differences appeared between novel and familiar sessions. Theta, alpha, beta and gamma power were significantly higher overall during novel sessions (Theta: Main Effect Novelty - $F(1,11) = 14.7$, $p = 0.003$, Mixed ANOVA; Alpha: Main Effect Novelty - $F(1,11) = 24.3$, $p = 4e-4$, Mixed ANOVA; Beta: Main Effect Novelty - $F(1,11) = 47.5$, $p = 3e-5$, Mixed ANOVA; Gamma: Main Effect Novelty - $F(1,11) = 19.9$, $p = 0.001$, Mixed ANOVA). There was a significant interaction between the effects of genotype and novelty on delta power (Interaction - $F(1,11) = 8.3$, $p = 0.01$, Mixed ANOVA). Delta power was significantly higher during novel sessions in J20 mice (Nov: 22.8 ± 0.2 dB; Fam: 21.8 ± 0.2 dB, p = 0.006), but not wild-type mice. Moreover, alpha and beta power were significantly higher overall in J20 mice (Alpha: Main Effect Genotype - $F(1,11) = 7.2$, $p = 0.02$, Mixed ANOVA; Beta: Main Effect Genotype - $F(1,11) = 21.9$, $p = 7e-4$, Mixed ANOVA). In order to demonstrate that the effect of novelty on spectral power was consistent across both novel sessions

(Day 1a and Day 5a), we statistically compared spectral power between these two sessions (Fig. 3). We found that there was no significant differences in spectral power between Day 1a and Day 5a for either wild-type or J20 mice, except for a small significant increase in alpha power in Day 5a compared to Day 1a in wild-type mice, when the entire session was analysed (Day 1a: 16.2 ± 0.3 dB; Day 5a: 16.7 ± 0.3 dB, $p = 0.04$). This result demonstrates that the effects of novelty on spectral power are not specific to a single session but occur equally during both exposures.

Across these time series, increased beta power occurred in brief, discrete epochs, as shown in the expanded power spectrogram in (Fig. 4a). This can also be seen clearly in beta-filtered local field potentials, where these periods of high beta amplitude intersperse an otherwise very low amplitude oscillation. In order to understand the timescale and frequency domains of these events, a continuous wavelet transform was performed using the Morse analytic wavelet, in order to investigate them further. As exemplified in (Fig. 4c), these individual events were short in duration, and peaked in the 20-30 Hz, beta band.

Beta Bursting Activity

In order to investigate this phasic beta activity in more depth, an algorithm was written to detect these epochs of high beta oscillatory amplitude, as described in the methods and illustrated in (Fig. 5a). With these transient epochs of high beta power now classified as discrete "beta bursts", it is possible to compare this beta activity between sessions. As shown in (Fig. 5b), there were significantly more beta bursts detected overall during novel sessions (Main Effect Novelty - $F(1,11) = 20.9$, $p = 8e\text{-}4$, Mixed ANOVA). Furthermore, there were significantly more beta bursts detected overall in J20 mice (Main Effect Genotype - $F(1,11) = 16.8$, $p = 0.002$, Mixed ANOVA). Furthermore, it is possible to investigate the distribution of beta bursts within sessions. As shown in (Fig. 5c, right), during familiar sessions the rate of beta busting was reasonably steady, as indicated by the linear relationship between time and burst number shown in the cumulative frequency plot, for both wild-type and J20 mice. During novel sessions, however, there was a high rate of beta bursting during the first 1-3 minutes of the session, which gradually decreased over time to a steady rate (Fig. 5c, left).

Beta bursting rate during the initial part of the session (first minute) and the final part of the session (last 10 minutes), was calculated for each session and averaged across novel and familiar sessions (Fig. 5d). The rate of beta bursting was significantly higher overall during novel sessions (Main Effect Novelty - $F(1,11) = 18.6$, $p = 0.001$, Mixed ANOVA), and also significantly higher overall during the initial part of recording sessions (Main Effect Time - $F(1,11) = 24.5$, $p = 4e\text{-}4$, Mixed ANOVA). During novel sessions, initial burst rate was significantly higher than final burst rate for wild-type (Nov Initial: 13 ± 1.6 bursts per minute; Final: 0.9 ± 0.1 bursts per minute, $p = 0.01$), and J20 mice (Nov Initial: 14.1 ± 3.6 bursts per minute; Final: 2.0 ± 0.4 bursts per minute, $p = 0.004$). Furthermore, there was no significant difference between wild-type and J20 mice for initial burst rate or final burst rate (Nov Initial - WT: 13 ± 1.6 bursts per minute; J20: 14.1 ± 3.7 bursts per minute, $p = 0.8$; Nov Final - WT: 0.9 ± 0.1 bursts per minute; J20: 2 ± 0.4 bursts per minute, $p = 0.08$). During familiar sessions, initial burst rate was significantly higher than final burst rate for J20 mice (Fam Initial: 5.1 ± 0.5 bursts per minute; Final: 2.1 ± 0.2 bursts per minute, $p = 1e\text{-}4$), but not wild-type mice (Fam Initial: 2.7 ± 0.5 bursts per minute; Final: 1.4 ± 0.1 bursts per minute, $p = 0.07$). Furthermore, initial burst rate and final burst rate were significantly higher in J20 mice than in wild-type mice (Fam Initial - WT: 2.7 ± 0.5 bursts per minute; J20: 5.1 ± 0.5 bursts per minute, $p = 0.006$; Fam Final - WT: 1.4 ± 0.1 bursts per minute; J20: 2.1 ± 0.2 bursts per minute, $p = 0.03$).

Beta Burst Characteristics

In order to attempt to understand the nature of retrosplenial beta bursts, and the mechanisms which underlie them, several beta burst characteristics were investigated. For each beta burst, the duration and magnitude were calculated, as shown in (Fig. 6a). Beta burst magnitude was significantly higher overall during novel sessions (Main Effect Novelty - $F(1,11) = 43.6$, $p = 4e\text{-}5$, Mixed ANOVA). As shown in (Fig. 6b), beta bursts were significantly larger in magnitude during novel sessions in wild-type (Nov: 93.3 ± 3 μV; Fam: 78.5 ± 2.7 μV, $p = 0.004$) and J20 mice (Nov: 121 ± 4.4 μV; Fam: 102 ± 3.3 μV, $p = 8e\text{-}5$). Moreover, beta bursts were significantly larger in magnitude overall in J20 mice (Main Effect Genotype - $F(1,11) = 14.3$, $p = 0.003$, Mixed ANOVA). Beta burst

duration was also significantly higher overall during novel sessions (Main Effect Novelty - $F(1,11) = 28.1$, $p = 3e\text{-}4$, Mixed ANOVA). As shown in (Fig. 6c), beta bursts were significantly longer in duration during novel sessions in wild-type (Nov: 190 ± 2.5 ms; Fam: 177 ± 1 ms, $p = 0.003$) and J20 mice (Nov: 189 ± 2 ms; Fam: 180 ± 0.9 ms, $p = 0.004$).

In order to understand the frequency profile of beta bursts, and to verify that these oscillations conformed to the beta frequency band (20-30 Hz), power spectral analysis was performed on individual beta bursts. As a control, these burst spectra were compared to power spectra of epochs of equal length directly prior to each burst. These power spectra were averaged across all bursts and "pre-bursts", for wild-type and J20 mice (Fig. 6d). Overall, beta bursts were associated with a large significant increase in beta power (Main Effect Burst - $F(1,11) = 4811$, $p = 7e\text{-}16$, Mixed ANOVA), and smaller significant increases in alpha and gamma power (Alpha: Main Effect Burst - $F(1,11) = 169$, $p = 5e\text{-}8$, Mixed ANOVA; Gamma: Main Effect Burst - $F(1,11) = 46$, $p = 3e\text{-}5$, Mixed ANOVA). Alpha, beta and gamma power were significantly higher during beta bursts in both wild-type (Alpha: WT – Pre-Burst: 16.5 ± 0.4 dB; Burst: 17.6 ± 0.3 dB, $p = 3e\text{-}6$; Beta: WT – Pre-Burst: 12.8 ± 0.3 dB; Burst: 19.9 ± 0.3 dB, $p = 9e\text{-}14$; Gamma: WT – Pre-Burst: 8.3 ± 0.2 dB; Burst: 8.6 ± 0.1 dB, $p = 0.002$), and J20 mice (Alpha: J20 – Pre-Burst: 17.7 ± 0.4 dB; Burst: 18.6 ± 0.4 dB, $p = 7e\text{-}7$; Beta: J20 – Pre-Burst: 15.2 ± 0.3 dB; Burst: 22.3 ± 0.3 dB, $p = 8e\text{-}15$; Gamma: J20 – Pre-Burst: 9.4 ± 0.2 dB; Burst: 9.8 ± 0.2 dB, $p = 1e\text{-}4$). Additionally, these findings confirm that these beta oscillations are not the merely the result of a harmonic of theta oscillations.

Running Speed Analysis

In order to investigate behavioural responses to novelty in this Novel/Familiar environment paradigm, we calculated each animal's running speed from the tracking data. Many previous studies have shown that environmental novelty is associated with increased exploration in rodents, as reflected by increased locomotor activity and therefore higher average running speeds (Dellu et al., 1996; Stone et al., 1999; Kabbaj et al., 2000), which would suggest that exploration should decrease in familiar environments, and that an absence of this decrease may indicate that this familiar

environment is being incorrectly perceived as novel. In order to test this, running speed was calculated from tracking data and averaged across the entire 15 minutes of both novel sessions (Day 1a and Day 5a), and the familiar sessions immediately following them (Day 1b and Day 5b) (Fig. 7a, left). At the time of the second session in each environment, animals will have only spent a total of 15 minutes in that environment, so uncertainty about whether the environment is novel or familiar would be most likely to manifest in these sessions. Conversely, by Day 4b animals will have spent a total of 2 hours in the first arena, so they should be able to recognise it with relative ease. Average running speed was significantly lower during familiar sessions in wild-type (Nov: 6.8 ± 0.3; Fam: 5.6 ± 0.4, $p = 0.04$), but not J20 mice (Nov: 8.0 ± 0.5; Fam: 7.8 ± 0.7, $p = 0.6$). Moreover, there was no significant overall difference between average running speed in wild-type and J20 mice (Main Effect Genotype - $F(1,12) = 3.1$, $p = 0.11$, Mixed ANOVA). As we have shown, neurophysiological responses to novelty are greatest during the first minute of recording sessions, so as before average running speed was also calculated for the first minute of both novel sessions (Day 1a and Day 5a), and the familiar sessions immediately following them (Day 1b and Day 5b) (Fig. 7a, right). There was a significant interaction between the effects of genotype and novelty on average running speed (Interaction - $F(1,12) = 6.8$, $p = 0.02$, Mixed ANOVA). Average running speed was significantly lower during the first minute of familiar sessions in wild-type (Nov: 8.4 ± 0.5; Fam: 4.8 ± 0.6, $p = 8.3e\text{-}4$), but not J20 mice (Nov: 9.6 ± 1.0; Fam: 8.8 ± 1.0, $p = 0.29$). Finally, average running speed during the first minute of familiar sessions was significantly higher in J20 mice than in wild-type mice (WT: 4.8 ± 0.6; J20: 8.8 ± 1.0, $p = 0.04$). These results suggest that J20 mice may have be experiencing some difficulty in discriminating whether their environment is novel or familiar

As we have shown, beta bursts are more prevalent during novel sessions, and both larger in magnitude and longer in duration, however it is unclear whether beta bursting varies with respect to the animal's movement speed. Hippocampal theta and gamma power have been shown to be positively correlated with running speed, so an increase in running speed may result in increased beta power during novel sessions (Chen et al., 2011; Ahmed and Mehta, 2012). In order to directly

investigate the relationships between beta bursting and running speed, we grouped beta bursts based on the animals running speed at the time of the burst. Firstly, in order to determine whether the prevalence of beta bursts increases with increased running speed, the average number of beta bursts detected in each running speed bin was divided by the average amount of time spent in each running speed bin, equivalent to the average beta burst rate at each running speed (Fig. 7b, left). In wild-type mice, beta bursts occurred at the same rate regardless of running speed ($R = -0.31$, $p = 0.39$), while in J20 mice beta bursts increased in prevalence with increasing running speed ($R = 0.78$, $p = 0.0079$). Secondly, in order to investigate potential relationships between beta burst characteristics and running speed, we calculated the average magnitude and duration of beta bursts across a range of running speed bins (Fig. 7c and d, respectively). Beta burst magnitude showed a clear linear relationship with running speed for both wild-type ($R = 0.96$, $p = 1.6e-5$) and J20 mice ($R = 0.93$, $p = 8e-5$). Furthermore, the pooled data in (Fig. 7c, right) shows that while average beta burst magnitude appeared to be higher overall in J20 mice, there was no significant difference in the slope or correlation coefficient of this relationship between the two genotypes (Slope - WT: 0.72 ± 0.24 µV/cm/s; J20: 0.57 ± 0.16 µV/cm/s; $t(11) = 0.53$, $p = 0.6$; unpaired t-test; R – WT: 0.44 ± 0.16; J20: 0.41 ± 0.12; $t(11) = 0.2$,$p = 0.9$; unpaired t-test). Conversely, as shown in (Fig. 7d, left), while there was a weak positive relationship between running speed and beta burst duration in J20 mice ($R = 0.72$, $p = 0.02$), this was absent in wild-type mice ($R = 0.03$, $p = 0.9$). Furthermore, the pooled data in (Fig. 7d, right) shows that there was no significant difference in the slope or correlation coefficient of this relationship between the two genotypes (Slope – WT: 0.03 ± 0.28 µV/cm/s; J20: 0.48 ± 0.2 µV/cm/s; $t(11) = -1.34$, $p = 0.2$; unpaired t-test; R – WT: 0.14 ± 0.08; J20: 0.15 ±0.05; $t(11) = -0.08$, $p = 0.9$; unpaired t-test). These data demonstrate increased beta bursting in J20 mice may, at least in part arise from a combination of a trend towards increased running speeds in these animals, and a positive correlation between beta bursting and running speed that is absent in wild-type mice. Conversely, while beta burst magnitude is positively correlated with running speed in both wild-type and J20 mice, the slope of this relationship is equivalent in both animals, suggesting that the trend

towards increased running speeds in J20 mice is unlikely to underlie higher average beta burst magnitudes in these animals.

Phase-amplitude Coupling

Phase-amplitude coupling (PAC) involves coupling between the amplitude of an oscillation and the phase of a lower frequency oscillation (Canolty et al., 2006). This interaction is generally thought to allow slow, large amplitude oscillations to coordinate faster, small amplitude local oscillations. Theta-gamma coupling is the most well studied form of PAC but PAC has been previously demonstrated for a range of other oscillation frequencies (Canolty et al., 2006; Tort et al., 2009; Daume et al., 2017). We investigated PAC across a range of frequencies in this study to determine whether retrosplenial PAC was associated with contextual novelty. Phase-amplitude coupling efficacy was calculated for a range of phase and amplitude frequencies, and the effect of novelty and genotype determined. As shown in (Fig. 8a), there were two large peaks in these comodulograms: one between theta phase and gamma amplitude, and another between theta phase and 12-30 Hz amplitude. This second peak did not conform to a single frequency band, and as such was treated as a composite of alpha and beta frequency. The strength of phase-amplitude coupling was quantified for theta-alpha/beta and theta-gamma coupling for each session (Fig. 8b). There was a significant interaction between the effects of genotype and novelty on theta-alpha/beta coupling (Interaction - $F(1,11) = 8.9$, $p = 0.01$, Mixed ANOVA). Theta-alpha/beta coupling was significantly higher during novel sessions for wild-type (Nov: 2.9 ± 0.1; Fam: 1.6 ± 0.1, $p = 4e\text{-}4$), but not J20 mice (Nov: 2.3 ± 0.2; Fam: 2 ± 0.2, $p = 0.15$). There were no significant effects of novelty or genotype on theta-gamma coupling (Main Effect Novelty - $F(1,11) = 0.2$, $p = 0.7$, Mixed ANOVA; Main Effect Genotype - $F(1,11) = 0.7$, $p = 0.4$, Mixed ANOVA). It is important to note that in order to focus on the most physiologically and behaviourally relevant part of the session, this analysis was performed for the first minute of each session. When the same analysis was performed on the last minute of each session, there was no effect of genotype or novelty on coupling on either theta-alpha/beta coupling (Main Effect Genotype - $F(1,11) = 0.4$, $p = 0.56$, Mixed ANOVA; Main Effect Novelty - $F(1,11) = 4.6$, $p = 0.054$,

Mixed ANOVA; Fig. 9b, left) or theta-gamma coupling (Main Effect Genotype - $F(1,11) = 3.7$, $p = 0.08$, Mixed ANOVA; Main Effect Novelty - $F(1,11) = 0.2$, $p = 0.69$, Mixed ANOVA; Fig. 9b, right).

Multi-Unit Activity

In order to determine whether beta bursting was associated with a change in neuronal firing, multi-unit activity was investigated. Due to the linear geometry of the silicon probes, and the 100 µm distance between channels, it was not possible to reliably identify single unit activity, as activity from a single neuron was unlikely to appear on multiple channels, limiting spatiotemporal clustering methods such as those enabled by tetrodes or higher density silicon probes. Therefore, spikes appearing on a single channel could be from one or more nearby neurons. This, however, does mean that it is possible to treat each individual probe channel as a single multi-unit, to facilitate investigation of the relationship between neuronal spiking activity and beta bursting. As shown in (Fig. 10a, left), individual spike waveforms can be readily discerned, and there was no significant difference in the mean amplitude of these waveforms between wild-type (black) and J20 (green) mice (WT: -90.3 ± 6.4 µV; J20: -82 ± 7.7 µV; $t(11) = -0.8$, $p = 0.5$; unpaired t-test). Furthermore, as shown in (Fig. 10a, right), there was no significant difference between average firing rate in wild-type and J20 mice (WT: 46.7 ± 10.1 Hz; J20: 43 ± 10.5 Hz; $t(11) = 0.24$, $p = 0.8$; unpaired t-test). Given that beta bursting in wild-type mice appears to be associated with increased neuronal spiking, it was of interest to investigate whether there was also a broad increase in the rate of neuronal spiking during this same time period. As shown in (Fig. 10b), during both novel (left) and familiar sessions (right), the rate of neuronal spiking was reasonably steady, as indicated by the linear relationship between time and spike number shown in the cumulative frequency plot, for both wild-type and J20 mice. The rate of neuronal spiking during the initial part of the session (first minute) and the final part of the session (last 10 minutes), was calculated for each session and averaged across novel (Fig. 10c, left) and familiar sessions (Fig. 10c, right). The rate of neuronal spiking was significantly higher overall during familiar sessions (Main Effect Novelty - $F(1,11) = 8.3$, $p = 0.02$, Mixed ANOVA), and also significantly higher overall during the final part of recording sessions (Main Effect Time - $F(1,11)$

519 = 21.4, p = 7e-4, Mixed ANOVA). During novel sessions, final spike rate was significantly higher than
520 initial spike rate for J20 mice (Nov Initial: 29.1 ± 7.0; Final: 41.9 ± 10.0, p = 0.002), but not wild-type
521 mice (Nov Initial: 37.7 ± 9.5 Hz; Final: 46.3 ± 11 Hz, p = 0.06). Furthermore, there was no significant
522 difference between wild-type and J20 mice for initial spike rate or final spike rate (Nov Initial - WT:
523 37.7 ± 9.5 Hz; J20: 29.1 ± 7.0 Hz, p = 0.5; Nov Final - WT: 46.3 ± 11 Hz; J20: 41.9 ± 9.9 Hz, p = 0.8).
524 During familiar sessions, final spike rate was significantly higher than initial spike rate for both wild-
525 type (Fam Initial: 41.6 ± 9.3 Hz; Final: 48.3 ± 10.2 Hz, p = 0.03), and J20 mice (Fam Initial: 37.7 ± 9.8
526 Hz; Final: 45.8 ± 11.2 Hz, p = 0.003). Furthermore, there was no significant difference between wild-
527 type and J20 mice for initial spike rate or final spike rate (Fam Initial - WT: 41.6 ± 9.3 Hz; J20: 37.7 ±
528 9.8 Hz, p = 0.8; Fam Final - WT: 48.3 ± 10.2 Hz; J20: 45.8 ± 11.2 Hz, p = 0.9). These data show that
529 while the rate of beta bursts is higher during novelty, the rate of neuronal spiking in the retrosplenial
530 cortex is higher during familiarity.
531 The average beta amplitude during beta bursts is shown in (Fig. 10d, top), averaged across all bursts
532 with non-overlapping time segments. Beta bursts in both genotypes are associated with a brief,
533 monophasic increase in beta amplitude that lasts no more than 200 ms on average. Finally, (Fig. 10d,
534 bottom) shows peri-event time histograms for spike rate during beta bursts, as a Z score from the
535 pre-burst epoch (left of the dotted line). In order to investigate potential statistically significant
536 changes in spike rate during beta bursts, we calculated the average z-scored spike rate between 0
537 and 250 ms after burst onset. Beta bursting in the RSCdg of wild-type mice was associated with a
538 significant increase in spike rate during beta bursts (Mean Z-scored spike rate: 0.9 ± 0.3; t(4) = 2.9, p
539 = 0.04; one-sample t-test; Fig. 10d, bottom left). Conversely there was no significant increase in
540 spike rate during beta bursts in J20 mice (Mean Z-scored spike rate: 0.48 ± 0.53; t(7) = 0.9, p = 0.4;
541 one-sample t-test; Fig. 10d, bottom right). These data suggest that beta bursts are coupled to
542 neuronal spiking in RSCdg in wild-type mice, and that this relationship is lost in J20 mice.
543 As we have shown, in wild-type mice beta bursting is associated with increased neuronal spiking in
544 the retrosplenial cortex, so in order to better understand the relationship between beta oscillations

and neuronal spiking, we performed additional analyses. Firstly, we investigated potential correlations between beta burst characteristics and their effect on neuronal spiking. There was no linear relationship between the change in spiking rate during beta bursts and the magnitude of the burst for either wild-type ($R = -0.082$, $p = 0.0065$) or J20 mice ($R = -0.0039$, $p = 0.84$). Conversely, there was a weak negative correlation between the change in spiking rate during beta bursts and the duration of the burst for both wild-type ($R = -0.3$, $p = 2.2e-24$) and J20 mice ($R = -0.22$, $p = 4.1e-30$). Secondly, we investigated potential phase-locking of neuronal spiking to a specific phase of the beta oscillation, which would support the idea that beta oscillations in the retrosplenial cortex are generated locally and not merely volume conducted from another region of the brain (França et al., 2021). For each recording session, histograms showing the probability of neuronal spiking at different phases of the beta oscillation were generated, and Rayleigh's test was performed on these individual phase histograms to investigate potential non-uniformity of these distributions. As shown in (Fig. 11c), neuronal spiking in both wild-type (top) and J20 mice (bottom) did not occur uniformly throughout the beta cycle, with increased spiking probability during the rising phase of the beta oscillation. The distribution of these significance levels is shown in (Fig. 11d, top), as the natural logarithm of Rayleigh's Z statistic, which itself is equivalent to the negative natural logarithm of p. The vertical red line shows the equivalent of $p = 0.05$, so all sessions to the right of this line demonstrate significant beta-phase locking, quantified in the pie charts below. Beta phase-locking of neuronal firing was seen in approximately 90% of sessions for both genotypes. Finally, the histograms in (Fig. 11e) show the distribution of preferred phase (μ, top) and concentration (κ, bottom) parameters for all significantly beta phase-locked sessions. Retrosplenial cortex spikes tended to occur at around 0°, during the rising phase of the beta oscillation, which was consistent across genotypes, while increased concentration (κ) values in J20 mice suggest a stronger degree of modulation in these animals. These results demonstrate that while there is no discernible relationship between the magnitude of beta bursts and neuronal spiking, the change in the rate of neuronal spiking during beta bursts appears to be higher during shorter beta bursts. Furthermore,

the presence of significant beta phase-locking of neuronal spiking suggests that beta oscillations are generated locally in the retrosplenial cortex.

Immunohistochemistry

In order to confirm the presence of age-related amyloid pathology in our J20 mice, we stained brains using Amylo-Glo (Biosensis, Schmued et al., 2012), a fluorescent marker which binds to amyloid plaques. We stained coronal slices from a subset of our 7-8-month-old experimental cohort, as well as an additional cohort of 12-13-month-old, J20 mice and wild-type littermates. Amylo-Glo staining revealed a high density of amyloid plaques in both the retrosplenial cortex and hippocampus of 12-13-month old J20 mice (Fig. 12b), and a complete absence of amyloid plaques in age-matched wild-type littermates (Fig.12a). Amyloid plaques seemed to vary greatly in size and density and were found in greatest number in the molecular layers of the dentate gyrus. 7-8-month old J20 mice had far fewer amyloid plaques, which were generally limited to the hippocampus. Quantification of amyloid plaques supported our findings of an age-related increase in amyloid plaque burden (Main Effect Age - $F(1,4) = 13.6$, $p = 0.02$, Mixed ANOVA, Fig. 12e), and an overall higher number of plaques in the hippocampus, compared to the retrosplenial cortex (Main Effect Region - $F(1,4) = 8.4$, $p = 0.04$, Mixed ANOVA, Fig. 12e), however this regional difference was only significant for the younger age group (Young - RSC: 0.7 ± 0.3; HC: 1.3 ± 0.2, $p = 0.02$).

The generation of fast oscillations such as gamma oscillations is thought to involve the activity of fast-spiking parvalbumin-positive interneurons (Csicsvari et al., 2003; Buzśaki and Wang, 2012), and parvalbumin-positive interneuron dysfunction is thought to underlie some of the neuronal network disturbances in Alzheimer's disease (for review, see Xu et al., 2020). In order to investigate whether the altered neuronal network activity in the retrosplenial cortex in J20 mice may be explained, at least in part by changes in the number of parvalbumin-positive interneurons in this region, we performed parvalbumin staining on brains from a group of 12-month-old wild-type and J20 mice (Fig. 13). Overall, the number of parvalbumin-positive interneurons was significantly higher in the dysgranular retrosplenial cortex than the granular retrosplenial cortex (Main Effect Region - $F(1,7) =$

56.5, p = 1.3e-4, Mixed ANOVA, Fig. 13e). The number of parvalbumin-positive interneurons was significantly higher in the dysgranular retrosplenial cortex than in the granular retrosplenial cortex for both wild-type (RSCdg: 32.3 ± 4.6; RSCg: 13.8 ± 2.8, p = 7.6e-4) and J20 mice (RSCdg: 33.4 ± 4.4; RSCg: 19 ± 2.9, p = 0.002). Conversely, there was no significant difference in the overall number of parvalbumin-positive interneurons in the retrosplenial cortex in wild-type and J20 mice (Main Effect Genotype - F(1,7) = 0.4, p = 0.5, Mixed ANOVA, Fig. 13e).

Discussion

In this study we attempted to identify neurophysiological correlates of environmental novelty in the mouse retrosplenial cortex (RSC), and investigate how these may be affected by amyloid pathology. We observed transient, high amplitude beta frequency oscillations, termed beta bursts, which occurred more frequently and with larger amplitude during novelty and were positively correlated with neuronal spiking. Several neurophysiological changes were seen in the RSC in J20 mice, many of them novel, which are indicative of aberrant neuronal network activity. These results together indicate that beta bursting activity is a neurophysiological correlate of environmental novelty in the RSC, which is disrupted in J20 mice and may underlie the apparent contextual memory impairments in these animals.

Numerous studies have noted changes in beta activity in a range of brain regions, during a variety of behaviours (see Spitzer and Haegens, 2017 for review). Berke *et al.* (2008) reported a large increase in beta power in the hippocampus when mice explore a novel environment, that persists for around a minute after exposure. The authors concluded that these oscillations may be a "dynamic state that facilitates the formation of unique contextual representations." Coherent 20-40 Hz oscillatory activity between the hippocampus and lateral entorhinal cortex has been shown to increase during odour discrimination, with the development of odour-specific neural representations (Igarashi *et al.,* 2014). Work by França *et al.* (2014) demonstrated that beta power was also transiently enhanced in the hippocampus during exploration of novel objects, but not familiar objects. Furthermore, they found that administration of an amnestic agent, namely haloperidol, resulted in a similar increased

beta activity upon re-exposure to previously encountered objects, suggesting they had been "forgotten". Subsequently, França, Borgegius and Cohen (2020) investigated novelty-associated beta bursting in the hippocampus, prefrontal cortex and parietal cortex during environmental and object novelty. Novelty-associated increases in beta power were seen in the prefrontal cortex during environmental novelty, and authors demonstrated significant phase-amplitude coupling of delta and theta to beta oscillations, which increased during novelty. In the RSC we see strong coupling between theta phase and alpha/beta amplitude, which is significantly higher during novelty in wild-type mice, alongside weaker coupling between theta phase and gamma amplitude, which is unaffected by novelty. While theta-gamma coupling is well established (for review, see Canolty and Knight, 2010), far less is known about theta-alpha/beta coupling. Previous studies have demonstrated theta-beta PAC in humans, both in the hippocampus during a working memory task (Axmacher et al., 2010), and in the inferior temporal cortex during object novelty (Daume et al., 2017). Theta-gamma coupling is the dominant form of phase-amplitude coupling in the hippocampus and is thought to support memory processes (Colgin et al., 2009; Axmacher et al., 2010; Newman et al., 2013; Lega et al., 2016), so our findings suggest that theta-alpha/beta coupling may be the cortical equivalent of theta-gamma coupling, and support memory process during contextual novelty. If this is true, then the absence of novelty-associated increases in theta-alpha/beta coupling in J20 mice may therefore have detrimental effects on memory processes. Interestingly, previous studies into beta oscillations during novelty tend to view beta activity as continuous oscillations, rather than discrete events (Berke et al., 2008; França et al., 2014, 2020). This is despite Berke *et al.* (2008) noting that beta appears as pulses, and a brief mention of burst detection and characterisation by França *et al.* (2014). As demonstrated in this study, novelty-associated beta oscillations in the RSC conform well to a model of discrete, rhythmic bursts, where their rate, magnitude and duration can vary depending on environmental novelty. Due to the use of averaging across trials or long temporal segments, the phasic nature of transient oscillatory events can be easily lost. Furthermore, in the somatosensory cortex, beta synchronicity appears as short

649 events in both mice and humans; the features of which, such as duration and frequency range, are
650 highly conserved across tasks and species (Shin et al., 2017). Sherman et al. (2016) hypothesised that
651 transient beta oscillations may arise as a result of synchronous bursts of excitatory activity at the
652 proximal and distal dendrites of pyramidal neurons. Furthermore, computational modelling suggests
653 that continuous 10 Hz stimulation at these sites is sufficient to produce beta bursts, which could
654 explain the strong phase-amplitude coupling between theta and beta oscillations in this paper,
655 especially during novelty.
656 Many groups have previously shown that information may be rapidly represented and stored in the
657 RSC (Cowansage et al., 2014; Czajkowski et al., 2014; Koike et al., 2017; Vedder et al., 2017). Beta
658 oscillations have also been shown to carry a variety of different forms of contextual information in a
659 range of brain regions, and phasic increases in beta power during working memory maintenance
660 may represent reactivation of encoded information (Spitzer and Haegens, 2017). Supporting this is a
661 study in which the authors employed transcranial magnetic stimulation to activate a currently
662 unattended memory, as shown by an increase in content-specific beta activity (Rose et al., 2016).
663 The theory put forth by Spitzer and Haegens (2017), is that beta oscillations can activate and
664 reactivate neuronal ensembles to create and recall cortical representations. This theory is consistent
665 with the data shown in this study: high beta bursting activity during perceived novelty activates
666 neurons in the RSC, which may encode content about the novel environment, and subsequent beta
667 bursting may continuously reactivate these ensembles, further consolidating or altering this
668 representation. Recent breakthroughs in real-time burst detection and neurofeedback have made it
669 possible to artificially induce beta bursts in awake behaving animals, creating the possibility of
670 testing this hypothesis directly (Karvat et al., 2020).
671 Several neurophysiological changes were seen in the RSC in J20 mice. Increases in alpha and beta
672 power are suggestive of cortical hyperexcitability, which has been previously shown in this strain
673 (Palop et al., 2007; Palop and Mucke, 2009). We noted increases in the rate of beta bursting and
674 burst magnitude, and an absence of coupling between beta bursting activity and neuronal spiking in

J20 mice, potentially impairing the ability to form neuronal ensembles that represent information in the RSC. Interestingly, excessive beta bursting in the basal ganglia and cortex is associated with the severity of motor impairments in Parkinson's disease (for review, see Brittain et al., 2014). Amyloid plaque formation in J20 mice increases dramatically with age and is most severe in the hippocampus and RSC (Whitesell et al., 2019), however at the age point used in this study, amyloid plaques were sparse in the retrosplenial cortex. This does not preclude the presence other potentially toxic species of amyloid beta, such as oligomers, which have been detected in the hippocampus (Wright et al., 2013) and cortex (Castanho et al., 2020) of J20 mice prior to substantial plaque load, but suggests that functional deficits in these animals occur independent of plaque formation. At 4 months-of-age, J20 mice have demonstrated impaired spatial learning and memory in the Morris Water Maze (Cheng et al., 2007) and the radial arm maze (Wright et al., 2013). Functional disturbances and cognitive impairments may arise from interneuron dysfunction, which has been demonstrated in J20 mice and has been shown to lead to cortical network hypersynchrony and spontaneous epileptiform discharges in animals 4-7 months-of-age (Verret et al., 2012). Reduced excitability of parvalbumin-positive interneurons in the hippocampus of 30 day old J20 mice has been associated with impaired theta-gamma phase-amplitude coupling (Mondragón-Rodríguez et al., 2018), and while parvalbumin-positive interneuron function was not necessary for the generation of ripples in the hippocampus, they were necessary for the coupling of neuronal spiking to ripples (Xia et al., 2017). These findings suggest that interneuron dysfunction in our J20 mice may underlie the altered phase-amplitude coupling and the loss of coupling of neuronal spiking to beta bursting shown in this paper. Reduced interneuron function in J20 mice could result in disinhibition and therefore underlie increases in beta burst magnitude and alpha/beta power. While the total number of parvalbumin-positive interneurons in the retrosplenial cortex did not differ between wild-type and J20 mice, it is possible that interneuron function may be altered. Similarly, in a different mouse model of Alzheimer's disease Booth et al. (2016) found altered gamma oscillations in the medial entorhinal cortex, but to the total number of parvalbumin-positive interneurons in this region. Finally, while

beta power is higher and beta bursts are more prevalent and larger in amplitude in J20 mice, their relationships with novelty are preserved, which may allow for the preservation of some contextual memory function. These findings demonstrate a novel form of Alzheimer's disease (AD) related cortical dysfunction, which may underlie or exacerbate cognitive dysfunction seen in these mice, and in people with AD (Cheng et al., 2007; Verret et al., 2012; Wright et al., 2013).

In conclusion, phasic bursts of beta oscillations may be a functional means of activating neural ensembles to form and subsequently reactivate cortical representations. Dysregulated beta bursting and an uncoupling of beta bursting from spiking are suggestive of network dysfunction in J20 mice which may underlie cognitive impairments in these mice.

Figure 1. Experimental Design A. Diagrams of the recording arenas used for this study. Both are roughly equal sized, one is square, with black and white stripes along the walls and floor (left) and the other is cylindrical with plain brown floor and walls. B. Experimental procedure for the novel/familiar environment task. A mouse is placed in one of the recording arenas for two 15-minute sessions, referred to as sessions A and B, with a 15-minute break in their home cage between the two sessions. This is repeated in the same arena for 4 consecutive days, after which the arena is switched for the 5^{th} and final day. C. Single shank, 16 channel silicon probe electrodes were implanted in the retrosplenial cortex (green), so that they spanned the dysgranular (upper green section) and granular (lower green section) subregions. In order to verify the location of the electrodes, electrolytic lesions were made prior to perfusion, and slices were histologically prepared using Cresyl Violet stain. An example is shown (right).

Figure 2. Beta (20-30 Hz) power is significantly higher during novelty in the dysgranular retrosplenial cortex in wild-type and J20 mice.

A. Example power spectrogram for an entire novel session in a wild-type mouse. B. Average power spectra for the entire 15 minutes of all novel and familiar sessions, for wild-type and J20 mice. Frequency bands are marked with dashed lines (Delta: 1-5 Hz, Theta: 5-12 Hz, Alpha: 12-20 Hz, Beta: 20-30 Hz, Gamma: 30-100 Hz). Beta power was significantly higher during novel sessions in both wild-type ($p = 0.02$) and J20 mice ($p = 2e\text{-}5$). Moreover, beta power was significantly higher in J20 mice than in wild-type mice, during novel ($p = 0.001$) and familiar sessions ($p = 0.002$). C. Example power spectrogram shown in A, expanded to show the first 60 seconds of the session (before the white line). Short epochs of increased power in the 20-40 Hz range can be seen. D. Average power spectra for the first minute of all novel and familiar sessions, for wild-type and J20 mice. Beta power was significantly higher overall during novel sessions ($p = 3e\text{-}5$) and was significantly higher overall in J20 mice ($p = 7e\text{-}4$). (Data shown as mean ± SEM, WT: $n = 5$, J20: $n = 8$).

Figure 3. Power spectral changes due to novelty are consistent across both exposures.

A. Average power spectra for the entire 15 minutes of novel sessions Day 1a and Day 5a, for wild-type mice. Frequency bands are marked with dashed lines (Delta: 1-5 Hz, Theta: 5-12 Hz, Alpha: 12-20 Hz, Beta: 20-30 Hz, Gamma: 30-100 Hz). There were no significant differences between Day 1a and Day 5a for power in any frequency band, except for a small increase in alpha power in Day 5a compared to Day 1a ($p = 0.04$). B. Average power spectra for the entire 15 minutes of novel sessions Day 1a and Day 5a, for J20 mice. There were no significant differences between Day 1a and Day 5a for power in any frequency band. C. Average power spectra for the first minute of novel sessions Day 1a and Day 5a, for wild-type mice. There were no significant differences between Day 1a and Day 5a for power in any frequency band. D. Average power spectra for the first minute of novel sessions Day 1a and Day 5a, for J20 mice. There were no significant differences between Day 1a and Day 5a for power in any frequency band. (Data shown as mean ± SEM, WT: $n = 5$, J20: $n = 8$).

Figure 4. Retrosplenial local field potentials are marked by short, phasic increases in beta power, referred to as beta bursts.

A. Example power spectrogram showing transient increases in beta power. B. Local field potentials of data shown in A, both unfiltered (top), and filtered in the beta band (bottom), with the envelope amplitude in blue for clarity. The beta-filtered local field potential shows clear epochs of high beta amplitude, which intersperse a low amplitude continuous beta oscillation. C. Expanded trace of the dashed area shown in B (bottom), and a continuous wavelet spectrogram of this time series (bottom). Due to the high temporal resolution of wavelet-based methods, these periods of high beta amplitude can be seen to be brief, only lasting around 100-200 ms.

Figure 5. Beta bursting activity in the dysgranular retrosplenial cortex (RSCdg) is significantly higher during novelty.

A. Diagram illustrating how beta bursts were detected. B. Graph showing the average number of beta bursts detected in RSCdg in each session, for wild-type (black) and J20 mice (green). Novel sessions Day 1a and Day 5a are highlighted in blue for clarity. Significantly more beta bursts were detected during novel sessions than during familiar sessions ($p = 8e\text{-}4$). Moreover, significantly more beta bursts were detected overall in J20 mice ($p = 0.002$). C. Cumulative frequency graphs of beta bursts detected in novel (left) and familiar sessions (right), for wild-type and J20 mice. While beta bursting occurred monotonically during familiar sessions, during the first minute of a novel session, beta bursting was substantially increased. D. Graphs showing beta burst rate during novel (left) and familiar sessions (right), for wild-type and J20 mice. Burst rate was quantified for the initial minute of each session, and final 10 minutes. Beta burst rate was significantly higher overall during the initial minute of novel sessions than during the final 10 minutes of novel sessions for both wild-type ($p = 0.01$) and J20 mice ($p = 0.004$). (Data shown as mean ± SEM, WT: $n = 5$, J20: $n = 8$, $^*p < 0.05$).

769 Figure 6. Beta burst characteristics in the dysgranular retrosplenial cortex (RSCdg).

770 A. Diagram illustrating how the magnitude and duration of beta bursts were calculated. B. Graph
771 showing the average beta burst magnitude in RSCdg in each session, for wild-type and J20 mice. Beta
772 bursts were overall significantly larger in magnitude during novel sessions ($p = 4e-5$). Moreover, beta
773 bursts were also significantly larger overall in J20 mice ($p = 8e-5$). C. Graph showing the average
774 duration of beta bursts in RSCdg in each session, for wild-type and J20 mice. Beta bursts were overall
775 significantly longer in duration during novel sessions ($p = 3e-4$), however there was no significant
776 overall difference between beta burst duration in wild-type and J20 mice. D. Average power spectra
777 for beta burst, and pre-burst epochs. Beta bursts were associated with a large, significant increase in
778 beta power during beta bursts ($p = 7e-16$). (Data shown as mean ± SEM, WT: $n = 5$, J20: $n = 8$).

Figure 7. Beta bursting in the dysgranular retrosplenial cortex appears to be unrelated to the running speed of the animal.

A. Graphs showing the average running speed of wild-type and J20 mice during novel sessions (Day 1a and Day 5a) and the first familiar session in each arena (Day 1b and Day 5b), averaged across the whole session (left), and the first minute of each session (right). Across the whole session, average running speed was lower during familiar sessions than novel sessions in wild-type ($p = 0.036$), but not J20 mice ($p = 0.64$). Similarly, when only the first minute was considered, average running speed was lower during familiar sessions than novel sessions in wild-type ($p = 8.3e\text{-}4$), but not J20 mice ($p = 0.29$). B. Graphs showing the relationship between the rate of beta bursting and the animal's running speed, across a range of running speed bins (left), and pooled data with the individual slopes and Fisher Z-transformed correlation coefficients for each animal. The rate of beta bursting was uncorrelated with running speed in wild-type mice, however in J20 mice there was a strong positive correlation ($p = 0.0079$). C. Graphs showing the relationships between the average magnitude of beta bursts and the animals running speed (left), and pooled data with the individual slopes and Fisher Z-transformed correlation coefficients for each animal. Beta burst magnitude was positively correlated with running speed for both wild-type ($p = 1.6e\text{-}5$) and J20 mice ($p = 8e\text{-}5$). D. Graphs showing the relationships between the average duration of beta bursts and the animals running speed (left), and pooled data with the individual slopes and Fisher Z-transformed correlation coefficients for each animal. Beta burst duration was uncorrelated with running speed in wild-type mice, however in J20 mice there was a weak positive correlation ($p = 0.018$). (Data shown as mean ± SEM, WT: $n = 5$, J20: $n = 8$).

Figure 8. Theta-alpha/beta phase-amplitude coupling is increased in the dysgranular retrosplenial cortex (RSCdg) during the first minute of novel sessions.

A. Average comodulograms showing the strength of cross-frequency phase-amplitude coupling in RSCdg during the first minute of novel and familiar sessions, for wild-type and J20 mice. Note the presence of two peaks in the theta-alpha/beta and theta-gamma ranges (the boundaries of which are denoted by the dotted lines). B. Average MI in the theta-alpha/beta (left) and theta-gamma ranges (right), for each session, for wild-type (black) and J20 mice (green). Novel sessions Day 1a and Day 5a are highlighted in blue for clarity. Theta-alpha/beta coupling was significantly higher during novel sessions for wild-type ($p = 0.01$), but not J20 mice ($p = 0.15$). There was no significant effect of genotype or novelty on theta-gamma coupling ($p = 0.4$, $p = 0.7$, respectively). (Data shown as mean ± SEM, WT: $n = 5$, J20: $n = 8$).

Figure 9. Theta-alpha/beta phase-amplitude coupling in the dysgranular retrosplenial cortex (RSCdg) is unaffected by novelty during the final minute of novel sessions.

A. Average comodulograms showing the strength of cross-frequency phase-amplitude coupling in RSCdg during the final minute of novel and familiar sessions, for wild-type and J20 mice. Note the presence of two peaks in the theta-alpha/beta and theta-gamma ranges (the boundaries of which are denoted by the dotted lines). B. Average MI in the theta-alpha/beta (left) and theta-gamma ranges (right), for each session, for wild-type (black) and J20 mice (green). Novel sessions Day 1a and Day 5a are highlighted in blue for clarity. There was no significant effect of genotype or novelty on theta-alpha/beta coupling ($p = 0.56$, $p = 0.054$, respectively) or theta-gamma coupling ($p = 0.08$, $p = 0.69$, respectively). (Data shown as mean ± SEM, WT: $n = 5$, J20: $n = 8$).

Figure 10. Spiking activity in RSCdg is coupled to beta bursting in wild-type mice, but disrupted in J20 mice.

A. Average spike waveforms for multi-unit activity in wild-type (black) and J20 (green) mice (left) and graph of average firing rate for detected multi-units across all sessions (right). There was no significant difference between the mean amplitude of spike waveforms in wild-type and J20 mice ($p = 0.5$). Moreover, there was no significant difference between average firing rate in wild-type and J20 mice ($p = 0.8$). B. Cumulative frequency graphs of neuronal spikes detected in novel (left) and familiar sessions (right), for wild-type and J20 mice. Neuronal spiking occurs as a relatively steady rate throughout both novel and familiar recording sessions. C. Graphs showing the average spike rate during novel (left) and familiar sessions (right), for wild-type and J20 mice. Spike rate was quantified for the initial minute of each session, and final 10 minutes. The rate of neuronal spiking was significantly higher overall during familiar sessions ($p = 0.02$), and significantly higher overall during the final part of recording sessions ($p = 7e-4$). D. Graphs showing beta amplitude (top) and multi-unit activity spike rate (bottom) over time for beta bursts, time locked to the onset of the burst (dotted line), and averaged across all detected bursts, for wild-type mice (left) and J20 mice (right). Beta bursting was associated with a monophasic increase in beta amplitude that returns to baseline after around 250 ms. Spiking data is shown as Z score from baseline (pre-burst epoch) and averaged across all beta bursts with non-overlapping time segments. Dotted vertical line denotes the burst onset, while the solid horizontal line is shown to indicate the baseline of zero. Beta bursts were associated with a significant increase in spike rate in wild-type ($p = 0.04$), but not J20 mice ($p = 0.4$). (Data shown as mean ± SEM, WT: $n = 5$, J20: $n = 8$, $^*p < 0.05$).

Figure 11. The effect of beta bursting on neuronal spiking is generally unaffected by the characteristics of the beta burst.

A. Individual peri-event histograms of the data shown in (Fig. 10d), showing multi-unit activity spike rate during beta bursts, for all wild-type (top) and J20 mice (bottom). Data is shown as Z score from baseline (pre-burst epoch) and averaged across all beta bursts with non-overlapping time segments. Dotted vertical line denotes the burst onset, while the solid horizontal line is shown to indicate the baseline of zero. Increased neuronal spiking during beta bursts was consistent across wild-type mice. B. Scatter plots showing the change in spike rate during each beta burst against the magnitude (left) and duration (right) of each beta burst, for all detected beta bursts in wild-type (left) and J20 mice (right). There was no linear relationship between the change in spiking rate during beta bursts and the magnitude of the burst for either wild-type ($R = -0.082$, $p = 0.0065$) or J20 mice ($R = -0.0039$, $p = 0.84$). Conversely, there was a weak negative correlation between the change in spiking rate during beta bursts and the duration of the burst for both wild-type ($R = -0.3$, $p = 2.2e-24$) and J20 mice ($R = -0.22$, $p = 4.1e-30$). C. Probability distributions for neuronal spiking at different phases of the beta oscillation, averaged across all sessions for wild-type (top) and J20 mice (bottom). D. Distribution of log-transformed Rayleigh's Z statistics for each session (top), which denotes the significance of beta phase-locking and is equivalent to the negative natural logarithm of p. Vertical red line illustrates an approximate significance level of $p = 0.05$, therefore all sessions to the right of this line therefore demonstrate significant beta-phase locking, quantified in the pie charts below for wild-type (left) and J20 mice (right). E. Histograms showing the estimated preferred phase (μ, top) and concentration (κ, bottom) parameters for all significantly beta phase-locked sessions. Retrosplenial cortex spikes tended to occur at around 0°, during the rising phase of the beta oscillation, which was consistent across genotypes. Furthermore, increased concentration (κ) values in J20 mice suggest a stronger degree of modulation in these animals. (Data shown as mean ± SEM, WT: $n = 5$, J20: $n = 8$).

Figure 12. J20 mice undergo age-related deposition of amyloid plaques throughout the hippocampus and retrosplenial cortex.

A. Example photomicrograph of the hippocampus and retrosplenial cortex of a 12-13-month old wild-type mouse, stained with Amylo-Glo, and excited with 405 nm violet light. This image was taken under 10X magnification using a Nikon Eclipse N800 epifluorescence microscope (Nikon). Brain from wild-type mice are completely lacking in amyloid plaque pathology. B. Example photomicrograph of the hippocampus and retrosplenial cortex of a 12-13-month old J20 mouse, taken under the same conditions as A. Abundant amyloid plaque pathology can be seen throughout the hippocampus and retrosplenial cortex. The two regions highlighted are shown in greater detail in C and D, taken under 20X magnification using a confocal microscope (ThorLabs). C. Example amyloid plaque found in the dysgranular retrosplenial cortex. D. Example amyloid plaque found in the dentate gyrus of the hippocampus. Amyloid plaques in J20 mice were found in greatest number in the molecular layers of the dentate gyrus. E. Graphs showing the average number of amyloid plaques found in the retrosplenial cortex and hippocampus of 7-8-month-old (left) and 12-13-month-old (right) J20 mice and wild-type littermates, with individual animals shown as well. Plaque load was higher overall in 12-13-month-old J20 mice ($p = 0.02$), and higher overall in the hippocampus ($p = 0.04$). In 7-8-month old J20 mice, plaques could be found in the hippocampus, and to a lesser extent in the retrosplenial cortex ($p = 0.02$), but overall amyloid plaque load was low at this age point. (Data shown as mean ± SEM, 7-8-month-old WT: $n = 1$, 7-8-month-old J20: $n = 3$, 12-13-month-old WT: $n = 5$, 12-13-month-old J20: $n = 3$).

Figure 13. Parvalbumin-positive interneurons in the retrosplenial cortex of wild-type and J20 mice.

A. Example photomicrograph of the retrosplenial cortex of a 12-month old wild-type mouse, stained with a parvalbumin-specific antibody. This image was taken under 4X magnification using a Nikon Eclipse N800 epifluorescence microscope (Nikon). The area highlighted is shown under 10X magnification in B. In wild-type mice, parvalbumin-positive interneurons can be seen in low numbers throughout the retrosplenial cortex. C. Example photomicrograph of the retrosplenial cortex of a 12-month old J20 mouse, taken under the same conditions as A. The area highlighted is shown under 10X magnification in B. As in wild-type mice, parvalbumin-positive interneurons can be seen in low numbers throughout the retrosplenial cortex of J20 mice. Graph showing the average number of parvalbumin(PV)-positive interneurons in the dysgranular and granular retrosplenial cortex of 12-month-old J20 mice and wild-type littermates, with individual animals shown as well. While numbers of PV-positive interneurons were higher on average in the dysgranular retrosplenial cortex ($p = 1.4e-4$), there was no significant difference between numbers of PV-positive interneurons in the retrosplenial cortex in wild-type and J20 mice ($p = 0.5$). (Data shown as mean ± SEM, WT: $n = 4$, J20: $n = 5$).

References

Ahmed OJ, Mehta MR (2012) Running speed alters the frequency of hippocampal gamma oscillations. J Neurosci 32:7373–7383.

Ahnaou A, Walsh C, Manyakov NV, Youssef SA, Drinkenburg WH (2019) Early Electrophysiological Disintegration of Hippocampal Neural Networks in a Novel Locus Coeruleus Tau-Seeding Mouse Model of Alzheimer's Disease. Neural Plasticity.

Axmacher N, Henseler MM, Jensen O, Weinreich I, Elger CE, Fell J (2010) Cross-frequency coupling supports multi-item working memory in the human hippocampus. Proc Natl Acad Sci 107:3228–3233.

Berens P (2009) CircStat: A MATLAB Toolbox for Circular Statistics. J Stat Softw 31.

Berke JD, Hetrick V, Breck J, Greene RW (2008) Transient 23-30 Hz oscillations in mouse hippocampus during exploration of novel environments. Hippocampus 18:519–529.

Booth CA, Ridler T, Murray TK, Ward MA, de Groot E, Goodfellow M, Phillips KG, Randall AD, Brown JT (2016) Electrical and network neuronal properties are preferentially disrupted in dorsal, but not ventral, medial entorhinal cortex in a mouse model of tauopathy. J Neurosci 36:312–324.

Brittain JS, Sharott A, Brown P (2014) The highs and lows of beta activity in cortico-basal ganglia loops. Eur J Neurosci 39:1951–1959.

Buzśaki G, Wang XJ (2012) Mechanisms of gamma oscillations. Annu Rev Neurosci 35:203–225.

Campbell R (2021) raacampbell/shadedErrorBar.

Canolty RT, Edwards E, Dalal SS, Soltani M, Nagarajan SS, Kirsch HE, Berger MS, Barbare NM, Knight RT (2006) High gamma power is phase-locked to theta oscillations in human neocortex. Science (80-) 313:1626–1628.

Canolty RT, Ganguly K, Kennerley SW, Cadieu CF, Koepsell K, Wallis JD, Carmena JM (2010) Oscillatory phase coupling coordinates anatomically dispersed functional cell assemblies. Proc Natl Acad Sci U S A 107:17356–17361.

Canolty RT, Knight RT (2010) The functional role of cross-frequency coupling. Trends Cogn Sci

14:506–515.

Castanho I, Murray TK, Hannon E, Jeffries A, Walker E, Laing E, Baulf H, Harvey J, Bradshaw L, Randall A, Moore K, O'Neill P, Lunnon K, Collier DA, Ahmed Z, O'Neill MJ, Mill J (2020) Transcriptional Signatures of Tau and Amyloid Neuropathology. Cell Rep 30.

Chen Z, Resnik E, McFarland JM, Sakmann B, Mehta MR (2011) Speed controls the amplitude and timing of the Hippocampal Gamma rhythm. PLoS One 6.

Cheng IH, Scearce-Levie K, Legleiter J, Palop JJ, Gerstein H, Bien-Ly N, Puoliväli J, Lesné S, Ashe KH, Muchowski PJ, Mucke L (2007) Accelerating amyloid-β fibrillization reduces oligomer levels and functional deficits in Alzheimer disease mouse models. J Biol Chem 282:23818–23828.

Choo IH, Lee DY, Oh JS, Lee JS, Lee DS, Song IC, Youn JC, Kim SG, Kim KW, Jhoo JH, Woo JI (2010) Posterior cingulate cortex atrophy and regional cingulum disruption in mild cognitive impairment and Alzheimer's disease. Neurobiol Aging 31:772–779.

Colgin LL, Denninger T, Fyhn M, Hafting T, Bonnevie T, Jensen O, Moser M-B, Moser EI (2009) Frequency of gamma oscillations routes flow of information in the hippocampus. Nat 2009 4627271 462:353–357.

Cowansage KK, Shuman T, Dillingham BC, Chang A, Golshani P, Mayford M (2014) Direct Reactivation of a Coherent Neocortical Memory of Context. Neuron 84:432–441.

Csicsvari J, Jamieson B, Wise KD, Buzsáki G (2003) Mechanisms of gamma oscillations in the hippocampus of the behaving rat. Neuron 37:311–322.

Czajkowski R, Jayaprakash B, Wiltgen B, Rogerson T, Guzman-Karlsson MC, Barth AL, Trachtenberg JT, Silva AJ (2014) Encoding and storage of spatial information in the retrosplenial cortex. Proc Natl Acad Sci 111:8661–8666.

Daume J, Gruber T, Engel AK, Friese U (2017) Phase-amplitude coupling and long-range phase synchronization reveal frontotemporal interactions during visual working memory. J Neurosci 37:313–322.

De Sousa AF, Cowansage KK, Zutshi I, Cardozo LM, Yoo EJ, Leutgeb S, Mayford M (2019) Optogenetic

952 reactivation of memory ensembles in the retrosplenial cortex induces systems consolidation.
953 Proc Natl Acad Sci U S A 116:8576–8581.
954 Dellu F, Piazza P V., Mayo W, Le Moal M, Simon H (1996) Novelty-seeking in rats--biobehavioral
955 characteristics and possible relationship with the sensation-seeking trait in man.
956 Neuropsychobiology 34:136–145.
957 França ASC, Borgegius N, Cohen MX (2020) Beta2 oscillations in the hippocampal-cortical novelty
958 detection circuit. Cold Spring Harbor Laboratory.
959 França ASC, Borgesius NZ, Souza BC, Cohen MX (2021) Beta2 Oscillations in Hippocampal-Cortical
960 Circuits During Novelty Detection. Front Syst Neurosci 15.
961 França ASC, do Nascimento GC, Lopes-dos-Santos V, Muratori L, Ribeiro S, Lobão-Soares B, Tort ABL
962 (2014) Beta2 oscillations (23-30 Hz) in the mouse hippocampus during novel object recognition.
963 Eur J Neurosci 40:3693–3703.
964 Iaria G, Chen JK, Guariglia C, Ptito A, Petrides M (2007) Retrosplenial and hippocampal brain regions
965 in human navigation: Complementary functional contributions to the formation and use of
966 cognitive maps. Eur J Neurosci 25:890–899.
967 Igarashi KM, Lu L, Colgin LL, Moser MB, Moser EI (2014) Coordination of entorhinal-hippocampal
968 ensemble activity during associative learning. Nature 510:143–147.
969 Kabbaj M, Devine DP, Savage VR, Akil H (2000) Neurobiological correlates of individual differences in
970 novelty-seeking behavior in the rat: differential expression of stress-related molecules. J
971 Neurosci 20:6983–6988.
972 Karvat G, Schneider A, Alyahyay M, Steenbergen F, Tangermann M, Diester I (2020) Real-time
973 detection of neural oscillation bursts allows behaviourally relevant neurofeedback. Commun
974 Biol 3.
975 Koike BDV, Farias KS, Billwiller F, Almeida-Filho D, Libourel PA, Tiran-Cappello A, Parmentier R,
976 Blanco W, Ribeiro S, Luppi PH, Queiroz CM (2017) Electrophysiological evidence that the
977 retrosplenial cortex displays a strong and specific activation phased with hippocampal theta

during paradoxical (REM) sleep. J Neurosci 37:8003–8013.

Kullback S, Leibler R. (1951) On Information and Sufficiency. Ann Math Stat 22:79–86.

Kwapis JL, Jarome TJ, Lee JL, Helmstetter FJ (2015) The retrosplenial cortex is involved in the formation of memory for context and trace fear conditioning. Neurobiol Learn Mem 123:110–116.

Laczó J, Vlček K, Vyhnálek M, Vajnerová O, Ort M, Holmerová I, Tolar M, Andel R, Bojar M, Hort J (2009) Spatial navigation testing discriminates two types of amnestic mild cognitive impairment. 202:252–259.

Lega B, Burke J, Jacobs J, Kahana M. (2016) Slow-Theta-to-Gamma Phase-Amplitude Coupling in Human Hippocampus Supports the Formation of New Episodic Memories. Cereb Cortex 26:268–278.

Mikofski M (2021) polyfitZero - File Exchange - MATLAB Central.

Minoshima S, Giordani B, Berent S, Frey KA, Foster NL, Kuhl DE (1997) Metabolic reduction in the posterior cingulate cortex in very early Alzheimer's disease. Ann Neurol 42:85–94.

Mitchell AS, Czajkowski R, Zhang N, Jeffery K, Nelson AJD (2018) Retrosplenial cortex and its role in spatial cognition. Brain Neurosci Adv 2:239821281875709.

Mitra P, Bokil H (2008) Observed Brain Dynamics.

Mondragón-Rodríguez S, Gu N, Manseau F, Williams S (2018) Alzheimer's Transgenic Model Is Characterized by Very Early Brain Network Alterations and β-CTF Fragment Accumulation: Reversal by β-Secretase Inhibition. Front Cell Neurosci 12.

Morganti F, Stefanini S, Riva G (2013) From allo- to egocentric spatial ability in early Alzheimer's disease: A study with virtual reality spatial tasks. Cogn Neurosci 4:171–180.

Newman EL, Gillet SN, Climer JR, Hasselmo ME (2013) Cholinergic blockade reduces theta-gamma phase amplitude coupling and speed modulation of theta frequency consistent with behavioral effects on encoding. J Neurosci 33:19635–19646.

Palop JJ, Chin J, Roberson ED, Wang J, Thwin MT, Bien-Ly N, Yoo J, Ho KO, Yu GQ, Kreitzer A,

1004 Finkbeiner S, Noebels JL, Mucke L (2007) Aberrant Excitatory Neuronal Activity and
1005 Compensatory Remodeling of Inhibitory Hippocampal Circuits in Mouse Models of Alzheimer's
1006 Disease. Neuron 55:697–711.
1007 Palop JJ, Mucke L (2009) Epilepsy and cognitive impairments in alzheimer disease. Arch Neurol
1008 66:435–440.
1009 Quiroga RQ, Nadasdy Z, Ben-Shaul Y (2004) Unsupervised spike detection and sorting with wavelets
1010 and superparamagnetic clustering. Neural Comput 16:1661–1687.
1011 Rose NS, LaRocque JJ, Riggall AC, Gosseries O, Starrett MJ, Meyering EE, Postle BR (2016)
1012 Reactivation of latent working memories with transcranial magnetic stimulation. Science (80-)
1013 354:1136–1139.
1014 Schindelin J, Arganda-Carreras I, Frise E, Kaynig V, Longair M, Pietzsch T, Preibisch S, Rueden C,
1015 Saalfeld S, Schmid B, Tinevez JY, White DJ, Hartenstein V, Eliceiri K, Tomancak P, Cardona A
1016 (2012) Fiji: an open-source platform for biological-image analysis. Nat Methods 2012 97 9:676–
1017 682.
1018 Schmued L, Raymick J, Tolleson W, Sarkar S, Zhang YH, Bell-Cohn A (2012) Introducing Amylo-Glo, a
1019 novel fluorescent amyloid specific histochemical tracer especially suited for multiple labeling
1020 and large scale quantification studies. J Neurosci Methods 209:120–126.
1021 Sherman MA, Lee S, Law R, Haegens S, Thorn CA, Hämäläinen MS, Moore CI, Jones SR (2016) Neural
1022 mechanisms of transient neocortical beta rhythms: Converging evidence from humans,
1023 computational modeling, monkeys, and mice. Proc Natl Acad Sci U S A 113:E4885.
1024 Shin H, Law R, Tsutsui S, Moore CI, Jones SR (2017) The rate of transient beta frequency events
1025 predicts behavior across tasks and species. Elife 6.
1026 Siapas AG, Lubenov E V., Wilson MA (2005) Prefrontal Phase Locking to Hippocampal Theta
1027 Oscillations. Neuron 46:141–151.
1028 Spitzer B, Haegens S (2017) Beyond the status quo: A role for beta oscillations in endogenous
1029 content (RE)activation. eNeuro 4.

1030 Stone EA, Zhang Y, Rosengarten H, Yeretsian J, Quartermain D (1999) Brain alpha 1-adrenergic
1031 neurotransmission is necessary for behavioral activation to environmental change in mice.
1032 Neuroscience 94:1245–1252.
1033 Todd TP, Bucci DJ (2015) Retrosplenial Cortex and Long-Term Memory: Molecules to Behavior.
1034 Neural Plast 2015.
1035 Tort ABL, Komorowski RW, Manns JR, Kopell NJ, Eichenbaum H (2009) Theta-gamma coupling
1036 increases during the learning of item-context associations. Proc Natl Acad Sci U S A 106:20942–
1037 20947.
1038 Vann SD, Aggleton JP, Maguire EA (2009) What does the retrosplenial cortex do? Nat Rev Neurosci
1039 10:792–802.
1040 Vedder LC, Miller AMP, Harrison MB, Smith DM (2017) Retrosplenial Cortical Neurons Encode
1041 Navigational Cues, Trajectories and Reward Locations during Goal Directed Navigation. Cereb
1042 Cortex 27:3713–3723.
1043 Verret L, Mann EO, Hang GB, Barth AMI, Cobos I, Ho K, Devidze N, Masliah E, Kreitzer AC, Mody I,
1044 Mucke L, Palop JJ (2012) Inhibitory interneuron deficit links altered network activity and
1045 cognitive dysfunction in alzheimer model. Cell 149:708–721.
1046 Walsh C, Drinkenburg WHIM, Ahnaou A (2017) Neurophysiological assessment of neural network
1047 plasticity and connectivity: Progress towards early functional biomarkers for disease
1048 interception therapies in Alzheimer's disease. Neurosci Biobehav Rev 73:340–358.
1049 Whitesell JD, Buckley AR, Knox JE, Kuan L, Graddis N, Pelos A, Mukora A, Wakeman W, Bohn P, Ho A,
1050 Hirokawa KE, Harris JA (2019) Whole brain imaging reveals distinct spatial patterns of amyloid
1051 beta deposition in three mouse models of Alzheimer's disease. J Comp Neurol 527:2122–2145.
1052 Wright AL, Zinn R, Hohensinn B, Konen LM, Beynon SB, Tan RP, Clark IA, Abdipranoto A, Vissel B
1053 (2013) Neuroinflammation and Neuronal Loss Precede Aβ Plaque Deposition in the hAPP-J20
1054 Mouse Model of Alzheimer's Disease. PLoS One 8.
1055 Xia F, Richards BA, Tran MM, Josselyn SA, Takehara-Nishiuchi K, Frankland PW (2017) Parvalbumin-

positive interneurons mediate neocortical-hippocampal interactions that are necessary for memory consolidation. Elife 6.

Xu Y, Zhao M, Han Y, Zhang H (2020) GABAergic Inhibitory Interneuron Deficits in Alzheimer's Disease: Implications for Treatment. Front Neurosci 14.

A

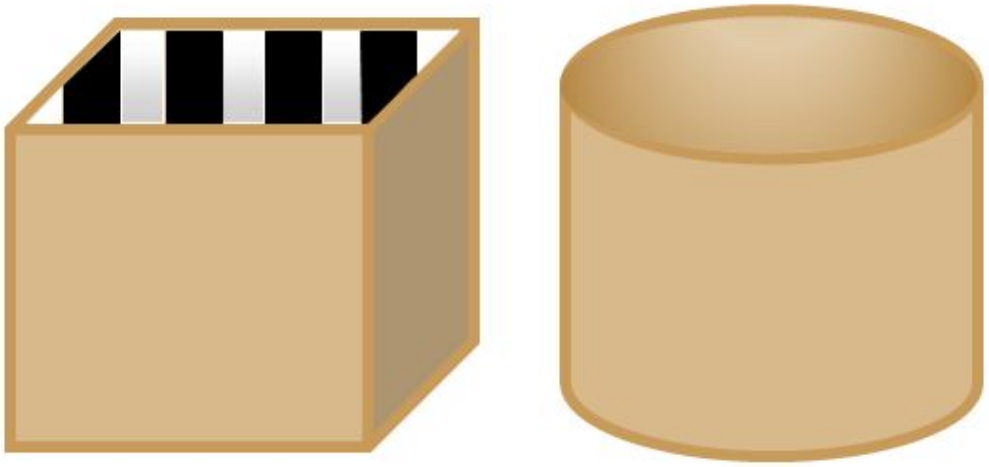

B

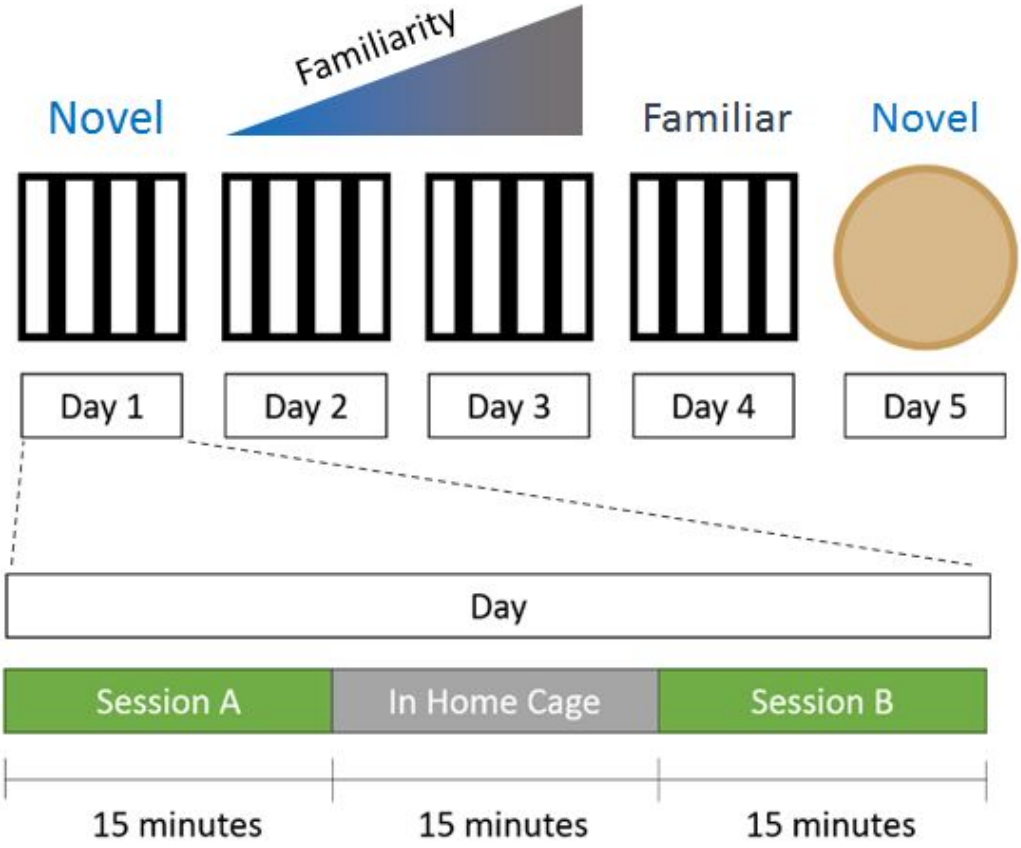

C